Effect of water and rock composition on re-strengthening of cohesive faults during the deceleration phase of seismic slip pulses

Violay M.[1], Passelegue F.[1], Spagnuolo E.[2], Di Toro G.[2,3], Cornelio C.[1]*

[1]Laboratory of Experimental Rock Mechanics EPFL, Lausanne, Switzerland

[2] Istituto Nazionale di Geofisica e Vulcanologia, Rome, Italy

[3] Dipartimento di Geoscienze, Università degli studi di Padova, Padua, Italy

*Corresponding author: marie.violay@epfl.ch

Abstract

The elastic strain energy release rate and seismic waves emitted during earthquakes are controlled by the on-fault temporal evolution of the shear stress during rupture propagation. High velocity friction experiments highlighted that shear stress on the fault surface evolves rapidly during seismic slip pulses. This temporal evolution of shear stress is controlled by both fault weakening at seismic slip initiation and re-strengthening rate towards the end of slip. While numerous studies focused on fault weakening, less attention was given to co-seismic re-strengthening processes. Here we performed 53 friction experiments (normal stress ≤30 MPa, slip-rate ≤6.5 m s^{-1}) imposing constant slip acceleration and deceleration (7.8 m s^{-2}), on cohesive Carrara marble (99% calcite) and micro-gabbro (silicate-built rock) under dry, vacuum and water pressurized conditions. Microstructural observations showed that micro-gabbro accommodated seismic slip by bulk melting of the sliding surfaces, whereas Carrara marble by coupled decarbonation and grain-size dependent crystal plastic processes. Under room humidity conditions and low imposed power density (i.e., product of normal stress per slip rate), re-strengthening rate during the deceleration stage was up to ~ 17 times faster in marble than in

micrograbbro. In the latter, the re-strengthening rate increased slightly with the power density. The presence of water enhanced further this trend. On the contrary, in marbles the re-strengthening rate decreased drastically with power density and in the presence of water. Our experimental observations highlighted the first order importance of the mineralogy and rheology of the slip zone materials and, to a second order, of the presence of water in controlling co-seismic re-strengthening of faults during seismic slip deceleration.

Keywords: Earthquake, Friction, Re-strengthening, Ground motions, Water effect.

1) Introduction:

Earthquakes are the result of sudden slip along faults, which releases the elastic strain and gravitational energy stored in the wall rocks [Reid, 1910; Scholz, 2002]. Damage associated with earthquakes is due to the radiation of elastic waves during seismic rupture propagation [Stein and Wysession, 2009, Marty et al., 2019] and to dynamic stress concentration at the rupture front [e.g., Andrews, 2005]. The intensity and the frequency of seismic waves (ground motions) are controlled by the rupture length and by the abrupt variations in rupture and slip velocities along fault during earthquakes [Brune, 1970; Madariaga, 1976]. Seismic rupture (~ km/s) and slip velocities (~ m/s) depend in particular on the temporal evolution of the shear stress along the fault during sliding (i.e., fault strength weakening and re-strengthening) [Ida, 1972; Ruina, 1983]. Friction experiments, performed with rotary shear machines designed to impose on rock specimens slip and slip rates typical of natural earthquakes, proved that experimental faults weakened due to several rock-type and environmental-dependent thermally activated weakening mechanisms, including melt lubrication, grain-size dependent processes, thermal and thermomechanical pressurization of pore fluids, etc. [Tsutsumi and Shimamoto, 1997; Di Toro et al., 2004; Han et al., 2010; Rice, 2006; Ferri et al., 2010; Di Toro 2011; Green

et al., 2015; De Paola et al., 2015; Spagnuolo et al., 2015; Violay et al., 2015]. Field studies of exhumed natural seismogenic faults support the evidence of rapid weakening and fault lubrication during earthquakes [Sibson, 1975; Di Toro et al., 2006]. The rheology of the fault is related to the physical state (e.g., liquid vs. solid) of the slipping zone [Rice, 2006], the slip rate and slip acceleration [Di Toro et al., 2004; Niemeijer et al., 2011; Chang et al., 2012], the rock composition [Di Toro et al., 2011; Goldsby and Tullis, 2011; Green et al., 2015], the presence of water [Violay et al., 2013; 2014], the ambient and local temperature [Lockner et al., 1986, Verberne et al., 2015], and in presence of non-cohesive rocks, on the gouge grain size [De Paola et al., 2015]. Indeed, in cohesive rocks, slip is highly localized from the very initiation of sliding and the rise of the temperature in the slipping zone increases with slip rate, effective normal stress and square root of the duration of sliding [e.g., Rice, 2006, Aubry et al., 2018]. In cohesive rocks, the abrupt increase in temperature favors "flash" heating and weakening mechanisms [Goldsby and Tullis, 2011] which may eventually evolve, for some silicate-built cohesive rocks, in bulk melting [Hirose et al., 2005; Niemeijer et al., 2011; Violay et al., 2013; Aubry et al., 2018]. On the contrary, in the presence of gouges, some slip is required before strain localization is achieved [Beeler et al., 1996; Marone 1990; Smith et al., 2015; Rempe et al., 2017; Pozzi et al., 2018]. As a consequence, heat production is more distributed in the slipping zone and other processes including thermal (if fluids are already present in the pores of the slipping zone) and thermomechanical (if fluids like CO_2 and H_2O are released by the breakdown of the minerals of the slipping zone) pressurization might be favored before bulk melting of the slipping zone occurs [e.g., Rice, 2006; Segall and Rice, 2006; Brantut et al., 2008; Ferri et al., 2010; Acosta et al., 2018].

While the physical parameters controlling fault weakening have been extensively studied, little attention has been dedicated on the processes associated to frictional re-strengthening observed during slip deceleration in seismic velocity pulses [Del Gaudio et al.,

2009; Chang et al., 2012; Liao et al., 2015; Proctor et al., 2014; Sone and Shimamoto, 2009]. However, fault strength evolution, i.e both strength weakening and re-strengthening, coupled with electrodynamic rupture propagation contributes actively to the slip rate evolution during seismic faulting and to the release of seismic waves [Sone and Shimamoto, 2009]. In addition, co-seismic re-strengthening processes controls the energy budget of earthquakes, as well as the transition from crack-like to pulse-like rupture, which implies a strong fault re-strengthening after the passage of the rupture front [Beeler and Tullis, 1998]. Few mechanisms of fault re-strengthening have been proposed so far: (1) temporal variation of stress conditions on the rupture interface during the passage of the rupture front (e.g., punctual pore fluid pressurization) [Lykotrafitis et al., 2006], (2) spatial variation of the initial stress field (barrier model) [Peyrat et al., 2001, Latour et al., 2011], (3) high dependence of friction to sliding velocity, i.e., "self-healing" behavior during sliding velocity deceleration [Beeler and Tullis, 1998; Sone and Shimamoto, 2009; Proctor et al., 2014; Perrin et al., 1995; Zheng and Rice, 1998]. Here, we present friction experiments that, by reproducing seismic slip conditions, aim at understanding the effect of rock composition and water content on fault re-strengthening during slip deceleration. In particular, we focused on cohesive rocks (calcitic marble and micrograbbro) where strain is localized from slip initiation to the final re-strengthening stage and the temperature evolution in the slipping zone is simpler than in case for non-cohesive rocks (gouges). Moreover, the analysis of the data reported here exploit the achievement of the so-called “steady-state” shear stress conditions in the experiments. This achievement requires slips of several centimeters to tens of centimeters depending on the applied effective normal stress [Di Toro et al., 2011]. Consequently, the results presented here should be valid for moderate to large in magnitude earthquakes, though steady-state conditions might not ever be achieved in nature [Liao et al., 2015]. The experimental evidences suggest that rock composition and

100 environmental conditions play a pivotal role in fault re-strengthening during seismic faulting,
101 with dramatic consequences in the radiation pattern of the emitted seismic waves.

102

103 2) Methods

104 We performed 53 high speed friction experiments on hollow cylinders (30/50 mm
105 internal/external diameter) of carbonate-built rock (Carrara marble, 99% calcite) and silicate-
106 bearing rock (micro-gabbro) (for sample preparation, see Nielsen et al., 2013). Carbonate-built
107 rocks and gabbros often host earthquakes sequences in nature, as attested by geological
108 evidence [Sibson, 1975]. The experiments were performed with SHIVA, a rotary shear machine
109 installed at the HP-HT INGV laboratories in Rome (see sup.mat.Table 1). SHIVA was equipped
110 with two brushless engines (max power 300 kW) and an air actuator (2000 kg amplified to 5000
111 kg thanks to a lever) in a rotary shear configuration to slid the two contacting hollow rock
112 cylinders under the desired conditions (Di Toro et al., 2010). Experiments were performed
113 either in the presence of pressurized liquid water, room humidity or under vacuum (10^{-4} mbar).
114 In the experiments with liquid water, SHIVA was equipped with a pressurizing system which
115 consisted of (1) a fluid pressure vessel (i.e., the samples were fully immersed in water), (2) a
116 membrane pump with a 30 cm^3 fluid capacity, (3) a pressure multiplier that imposes up to 15
117 MPa of fluid pressure (P_f), (4) a pressure regulator and, (5) valves and pipes [Violay et al.,
118 2013]. Normal stress (σ_n) and pore pressure (P_f) (drained conditions) were kept constant during
119 experiments to target values ranging between 10 and 40 MPa and 0 (nominally dry) and 15
120 MPa, respectively. To mimic the sliding velocity at a given point of the fault during propagation
121 and arrest of seismic slip, we imposed a trapezoidal slip velocity function by imposing constant
122 acceleration and deceleration (7.8 m s^{-2}) and target slip velocities ranging from 1 m s^{-1} to 6.5 m
123 s^{-1}. Total slip ranged from 0.83 m to 18.37 m.

Mechanical data (axial load, torque, axial displacement, and angular rotation) were acquired at a frequency up to 25 kHz (for description of the installed instrumentation, their calibration and acquisition rates, see Niemeijer et al., 2011). Normal stress, shear stress (τ) and slip velocity (V) were computed from experimental measurements following Tsutsumi and Shimamoto [1997] and Di Toro et al. [2010].

3) Results

In all the experiments, once the slip velocity function was applied, the apparatus and the sample initially deformed elastically until the static friction coefficient μ_p ($\mu = \tau/\sigma_n^{eff}$ with $\sigma_n^{eff} = \sigma_n - P_f$) was overcome and slip initiated (Fig. 1). Then, the friction coefficient decreased exponentially with slip over a weakening distance D_w down to a so-called steady-state friction coefficient μ_{ss}. Towards the end of the experiment, during slip velocity deceleration, the friction coefficient recovered with time and slip to a final value μ_r at the offset of slip (Figs.1a-b). The effects of rock composition and environmental conditions on fault weakening and μ_p, μ_{ss} and D_w were discussed in Violay et al. [2013 and 2014]. As well as for initial fault weakening [Di Toro et al., 2011], the recovery of the friction coefficient during the deceleration stage of the velocity pulse is a function of the sliding velocity (Figs.1c-d) [Goldsby and Tullis, 2011; Passelègue et al., 2014; Proctor et al., 2014]. The value of μ_r ranged from 0.08 to 0.63 for Carrara marble and 0.11 to 0.37 for micro-gabbro, respectively, and independently of (1) the environmental conditions, (2) the final slip and (3) of the initial power ($\sigma_n^{eff} V$) imposed on the fault (Figs. 2 and 3). To investigate the physics of the re-strengthening processes, we computed, for each experiment, the friction re-strengthening rate $\dot{\mu} = (\mu_r - \mu_{ss})/(t_r - t_{ss})$, where $(t_r - t_{ss})$ is the deceleration duration from end of the steady-state to the end of slip (Figs. 1a-b). At constant acceleration and deceleration rate, in the experiments conducted at low initial power density

148 (σ_n^{eff} V < 20 MW m^{-2}) and under both room humidity and vacuum conditions, the re-
149 strengthening rate was ~ 17 times faster in Carrara marble (from 2.00 to 3.68 s^{-1}) than in micro-
150 grabbro (from 0.02 to 0.16 s^{-1}) (Fig 4). In both rock types, re-strengthening rate was inital power
151 density-dependent and work density independent (i.e., slip independent) (Fig.4). In Carrara
152 marble, independently of the environmental conditions, the friction re-strengthening rate
153 decreased with increasing power density (Figs. 3-4). This trend was amplified in pressurized
154 water conditions, and at the largest power densities tested, re-strengthening rate became almost
155 negligible (Fig. 4a). The opposite behavior was observed in micro-gabbro. The re-strengthening
156 rate slightly increased with the power density, and this effect was amplified in presence of
157 pressurized water (Fig. 4b). Moreover, in Carrara marble the re-strengthening rate was about
158 two times (at low power density) slower in the presence of pressurized liquid water than under
159 room and vacuum conditions (Fig 4). Instead, in micro-gabbro, the frictional re-strengthening
160 rate was about three times faster in the presence of pressurized liquid water than under room
161 humidity and vacuum conditions (Fig 4). Therefore, pressurized liquid water had an opposite
162 effect on the frictional re-strengthening rate of Carrara marble with respect to the one of micro-
163 gabbro.

164 Regarding the microstructures, mineralogy and geochemistry of the slipping zones and
165 slip surfaces recovered after the experiments, we refer to previous studies performed (1) on
166 several samples from the experiments presented here [Violay et al., 2013; 2014] and (2) on
167 slipping zone produced in experiments conducted on similar rocks (e.g., gabbro, basalts and
168 Carrara marbles) under very similar deformation conditions [Han et al., 2010; Di Toro et al.,
169 2011]. In the case of micro-gabbro, the slipping zone consisted of a continuous ca. 200 μm thick
170 layer of a quenched melt (see composition in Table 2), independently of the presence or absence
171 of liquid water (Fig. 5a) [Violay et al., 2014; 2015; Nielsen et al., 2008; 2010; Niemeijer et al.,
172 2011; Giacomel et al., 2018]. In the case of the Carrara marble, the slipping zone after

experiments conducted under vacuum and room humidity consisted of a 50 to 100 μm thick layer of nano- to micro-grained, poorly cohesive material made of calcite and, to a minor extent, lime (Violay et al., 2013; Spagnuolo et al., 2015) (Fig. 5b). Unfortunately, due to the poorly cohesive nature of the nano- to micro-grained deformed layer, most of the slipping zone was flushed away during sample recovery in the experiments performed in the presence of liquid water. However, the few micro-fault patches recovered from the slip surface showed the presence of nano- to micro-grained slipping zones [Violay et al., 2013; 2015] and evidence of calcite decabonatation attested by the presence of vacuoles within the grains. Violay et al., [2013] also showed evidence of CO_2 increase in the fluids recovered after high-speed friction experiments performed on carbonate bearing rocks. We infer that also in the case of the experiments performed with Carrara marble, the slipping had the same microstructure independently of the presence or absence of liquid water.

4) Discussion

4.1) Effect of water on friction re-strengthening rate

The different effect of the presence of pressurized liquid water on the frictional re-strengthening rate of micro-gabbro and Carrara marble suggested that different micro-physical processes operated during the deceleration phase of the slip pulse, as clearly supported by microstructural evidence (Fig. 5). It is well-known that fault surfaces of micro-gabbro melt with seismic slip under room humidity and vacuum conditions [Tsutsumi and Shimamoto, 1997; Hirose and Shimamoto, 2005; Nielsen et al., 2008; Niemeijer et al., 2011], but also in the presence of liquid water [Violay 2014a; 2014b]. On the contrary, slipping zones of Carrara marble did not record microstructural evidence of frictional melting. Instead, the slipping zones were made of sub-micrometer to nanometer in size grains [Spagnuolo et al., 2015]. These microstructures can be associated to grain-size dependent crystal plastic processes [Green et al.,

198 2015; De Paola et al., 2015; Spagnuolo et al., 2015]. Similarly to what occurred during the
199 initial weakening stage, was the rheology of the materials building the slipping zone that
200 controlled the final frictional re-strengthening. In our experiments, the rheology of the slipping
201 zone depended on the physical state of the sheared materials (melt vs. nano-grains), on the slip
202 and strain rate, on the normal stress, as well as on the environmental conditions and, for Carrara
203 marble, on grain size.

204 In the case of micro-gabbro, the viscosity and thickness of the melt layer and its
205 extrusion rate from the slipping zone controlled the viscous strength of the experimental fault
206 [Nielsen et al., 2008]. Violay et al., [2014a] showed that the initial fault weakening by frictional
207 melts was delayed by the presence of liquid water that cools the asperity contacts. Here, we
208 hypothesize that frictional re-strengthening might be enhanced by an increase of the viscous
209 strength of the melt layer due to water-cooling. To test this hypothesis, we implemented a Finite
210 Element Methods numerical model which included the rock specimens and the steel-made
211 pressure vessel (Fig. 6 a, b, c). The slipping zone was modeled as a 200 μm-thick layer (red in
212 color in Fig. 6, a), consistently with the typical thickness of the solidified melt layers recovered
213 at the end of the experiments [Nielsen et al., 2008], made by melt plus water or melt plus air
214 with a constant volume ratio (ϕ) ranging from 0.5 to 0.9 in agreement with microstructural
215 observations [Brown and Fialko, 2002, Violay et al., 2014a; 2014b] (Fig. 5). The melt
216 temperature during slip deceleration was computed using the mechanical data of the samples
217 sheared under vacuum conditions as a reference. In fact, under vacuum conditions, most of the
218 frictional work was dissipated into heat (the contribution to wear and rock fragmentation was
219 negligible, see Niemeijer et al., 2011) and very limited heat was lost by radiation. Consequently,
220 the heat flux Q was a function of shear stress and slip rate that evolved with time t (Fig. 1) and
221 varied along the sample radius r:

222 $$Q(r,t) = 0.5 \cdot \tau(t) \cdot V(r,t) \qquad (Eq.1).$$

For experiments performed under room humidity conditions and in the presence of water, we imposed that the melt layer was cooled by air or water (2D heat diffusion model), respectively. Then, as representative of the entire slipping zone, we used the estimated temperature achieved by the friction melt at 2/3 of the sample radius. The properties of the slipping zone (indicated by the subscript $_{eff}$ for effective) were considered as a linear combination of the thermal properties of the fluid (air or water) and those of the melt (Table 1). Therefore, the "effective" thermal diffusivity in the slip zone was:

$$\alpha_{eff} = K_{eff} / (\rho C)_{eff} \qquad (Eq.2)$$

where

$$K_{eff} = (1 - \phi) K_R + \phi K_f \qquad (Eq.3)$$

and

$$(\rho C)_{eff} = (1 - \phi) \rho_R C_R + \phi \rho_f C_f \qquad (Eq.4)$$

with K, the thermal conductivity (W m^{-1} K^{-1}), C the specific heat capacity (J kg^{-1} K^{-1}), ρ the density (kg m^{-3}) and ϕ the liquid fraction in the melt. Index R and f are related to the rock and fluid properties, respectively. Then, the heat diffusion is:

$$\rho . C_{eff} . \frac{\partial T}{\partial t} = \nabla . \left(k_{eff,i} . T \right) \qquad (Eq.5)$$

where i represents the two different materials (water/air and rock) in the model of Fig. 6. Values of thermal conductivity, specific heat capacity and density are reported in Table 1. The melt viscosity (η) was computed with the viscosity simulator for silicate melts of Giordano et al., [2008] (we did not take into account the crystal fraction in the melt). The model predicts the non-Arrhenius temperature dependence of viscosity for naturally-occurring silicate melts at atmospheric pressure:

$$log(\eta) = A + \frac{B}{T(K) - C} \qquad (Eq.6)$$

where A is a constant independent of composition and B and C are adjustable parameters depending on melt composition. The glass chemical composition was published by Violay et al., [2014, sup mat item 4] and reported in Table 2. Numerical modelling results highlighted that the melt viscosity, because of cooling of the melt, increases with decreasing sliding velocity (Fig. 6), in agreement with the logarithmic increase of the "friction coefficient" during the deceleration stage (Figs. 1 and 3). In addition, the increase of melt viscosity during slip deceleration was significantly faster in experiments performed in the presence of pressurized water than under room humidity conditions, suggesting that water-cooling was an efficient mechanism of re-strengthening. Moreover, the efficiency of water-cooling was proportional to the fluid-to-melt ratio in the slipping zone, and therefore of the temperature of the melt before deceleration. Indeed, higher was the melt temperature at the steady-state, which was slightly proportional to the imposed power density, faster was the increase of melt viscosity during slip deceleration. Instead, given the same conditions, the observation that the re-strengthening rate was independent of slip (Figs. 4d) was related to the large shortening rate of the rock specimens during frictional melting (mm per meters of slip, Violay et al., 2014). At steady-state conditions, the isotherms were almost fixed in space while the rock specimen passes through them and got melted and extruded (see discussion in Nielsen et al., 2008). As a consequence, once steady-state had been achieved (always the case for the experiments presented here), during deceleration and melt cooling, the wall rocks were at similar temperatures independently of the cumulated slip and the re-strengthening is independent of slip.

In the case of Carrara marble, the slower re-strengthening rate in the presence of water than under room humidity conditions (Fig. 4a) cannot be explained by water cooling of the slipping zone or by thermal fluid depressurization (i.e., fluid pressure decrease after a short period of expansion caused by frictional heating). Indeed, neither melt was produced nor pressurization was observed during these experiments where fluid pressure was kept constant

271 under drained conditions [Violay et al., 2015]. Moreover, both melt lubrication and thermal
272 pressurization would lead to a faster re-strengthening in presence of water than under room
273 humidity conditions. However, this is at odds with the experimental evidence: re-strengthening
274 rate is faster under vacuum conditions (Fig4). Note also that calcite decarbonation as potential
275 re-strengthening mechanism can be ruled out in our experiments. This mechanism would led to
276 faster re-strengthening at high power density (i.e., higher temperature), which it is just the
277 opposite of our experimental evidence.
278 We suggest that the slower recovery of the frictional strength in the presence of liquid water
279 during slip deceleration can be due to the strain rate sensitive, grain size dependent crystal
280 plasticity of calcite in the presence of water (e.g.. grain boundary sliding aided by diffusion
281 creep) [Rutter, 1974, Schmidt et al., 1980, 1987, Walker et al., 1990, Renner et al., 2002].
282 Decarbonation reaction can propably help this mechanism because it triggers the formation of
283 nanoparticles allowing the activation of grain size depend processes. Despite relevant
284 differences between our experimental protocol and those reported in the above-mentioned
285 studies (high pressure - high temperature triaxial tests performed at very low strain rates, 10^{-6}-
286 10^{-4} s^{-1}, compared to those achieved in our experiments, 10^{2}-10^{4} s^{-1}), a comparison with those
287 studies may help to understand better the mechanisms accommodating deformation in our
288 experiments. At high temperature (> 400°C), calcite strength is temperature and strain rate
289 dependent [Rutter, 1971, 1974], and governed by crystal-plastic and grain size-dependent
290 deformation mechanisms (intracrystalline plasticity and grain boundary sliding diffusion-
291 assisted plasticity). Similar deformation mechanisms were inferred to be operating at sub-
292 seismic and seismic slip rates in calcite [Verberne et al., 2015; De Paola et al., 2015; Spagnuolo
293 et al 2015]. Rutter [1972] showed that calcite strength is inversely proportional to water content
294 due to the reduction of the surface energy at calcite grain boundaries [Boozer et al., 1962] and
295 its strain rate sensitive behavior decreased with increasing water content. Rutter [1974] had also

shown that water effect is relatively small in Carrara marble. If crystal-plastic and grain-size dependent processes were triggered during high velocity friction experiments, they would therefore result in a negative dependence of strain-rate on residual flow stress, and may explain the inhibition of the frictional re-strengthening in Carrara marbles especially at large power densities. In fact, for larger power densities, higher temperatures should be achieved in both the slipping zone and wall rocks. This should be the case especially once the so-called steady-steady conditions were achieved (note that, because of the power-law decay in Carrara marble, "steady-state" conditions remain an approximation, see Nielsen et al., 2016). In fact, because of the absence or negligible shortening of the marble specimens, contrary to what happens in micro-gabbro, heat diffused in the wall rocks. Hotter wall rocks and the different deformation mechanism involved would result in slower cooling of the slipping zone, especially if compared to the frictional melting case (compare Fig. 4a with 4b). In the presence of water, the efficiency of grain size dependent and diffusion-controlled processes should be enhanced due to lower activation energy in presence of water, explaining the lower re-strengthening rate. However, the slipping zone was flushed away at the end of slip preventing sample recovery for micro-analytical investigations [Violay et al., 2013, 2014]. To test this hypothesis, we performed a one dimension-time dependent diffusion temperature model fully coupled with grain-size diffusion creep flow law (Fig.7). Calcite thermal properties are reported on Table 1. The slipping zone was modeled by a 100 µm- layer composed of 100 nm grain size calcite, in agreement with microstructural observations [Violay et al., 2013, 2015] (Fig.5). The heat flux and diffusion were computed following Eq.1 and 5. The predicted flow stress for diffusion creep plasticity can be modelled by the constitutive flow law (Eq. 8, 9).

$$\frac{\partial T}{\partial t} = \frac{1}{2}\tau(t)V(t) + \frac{k}{C_p\rho}\frac{\partial^2 T}{\partial x^2} \quad \text{(eq.7)}$$

$$\tau(t) = \left(\frac{\dot{\gamma}}{\left(A \cdot D^{-b} e^{-\frac{H}{RT(t)}}\right)}\right)^{\frac{1}{n}} \quad \text{(eq.8)}$$

$$\dot{\gamma} = \frac{1}{l}\frac{\partial V}{\partial t} \quad \text{(eq.9)}$$

where $\dot{\gamma}$ is the shear strain rate, A the pre-exponential factor, H the apparent activation energy for creep, R the gas constant, T the temperature, τ the shear stress at time step (t), n the stress exponent, D the grain size with b the grain size exponent, l is the layer thickness, and $V(t)$ is the slip velocity function.

Following [De Paola et al., 2015], under room-humidity conditions, b= 2, n=1, H=217 kJ mol^{-1}, A=9.55 *10^5 (s^{-1}. Bar^{-n})., R=8.314 J.K.mol^{-1}. In presence of water, we supposed a reduction of the activation energy (H) of about 20% , with H=176 Kj kJ mol^{-1} (see discussion in Rutter 1972). Flow stress estimates based on Eqs.7,8,9 (Fig.7) showed that grain boundary sliding aided by diffusion mechanism can explained both the strength weakening at the beginning of the experiments, the steady state friction and the final re-strengthening. Moreover, a decrease of the activation energy of only 20% under pore fluid conditions [Rutter, 1972] may justify the faster re-strengthening observed under dry rather than under pore fluid conditions (Fig. 1c).

4.2) Implications for natural earthquakes

Our experiments demonstrated that the slip deceleration can result in rapid fault re-strengthening, up to 10 to 90% of the initial peak stress, depending on the rheology of the material building the slip zone which depends on lithology and environmental conditions (Fig. 1). Because the friction coefficient is strongly velocity-dependent [Sone and Shimamoto, 2009], the magnitude of the re-strengthening depends mainly on the imposed deceleration rate [Del Gaudio et al., 2009]. The extrapolation of these results to natural earthquakes can be gained by (1) comparing the friction re-strengthening rate between experiments performed with different rock types and under environmental conditions, and (2) using the dependency of the re-strengthening rate with the power density.

Here below, we estimate the slip-velocity, acceleration and power density of natural earthquakes and compare them to the imposed parameters during our experiments. Slip-velocity functions during earthquake rupture propagation are obtained by inverting ground motion waveforms. Slip acceleration and deceleration during earthquakes are ~1-10 m s^{-2} (and larger, Tinti et al., 2005) and slip rates, on average, ~ 1 m s^{-1} [Heaton, 1990]. Therefore, acceleration, deceleration as well as slip-velocity imposed in our experiments are somehow comparable to those of natural earthquakes. The main differences between tests and earthquakes are in the shape of the velocity function (trapezoidal in our case) and on the normal stress imposed. Indeed, crustal earthquakes nucleate between 5 and 15 km depth, possibly at effective normal stresses of ~100-200 MPa [Zoback and Harjes, 1997], and at power densities perhaps up to ten times higher than those imposed in the experiments discussed here. Extrapolation of our results to realistic stresses conditions suggest that in cohesive carbonate-bearing rocks, frictional re-strengthening during slip-velocity deceleration is probably almost negligible whereas in cohesive silicate bearing-rocks, re-strengthening processes are highly deceleration-dependent, especially in the presence of water.

Indeed, our results demonstrate that, due to the large expected power densities during natural earthquakes, small variations in the slip velocity could induce strong variations in friction promoting further changes in the slip velocity history due to co-seismic re-strengthening, especially in the case of calcite-built rocks. Moreover, the frequency content of the radiated energy is affected by the abruptness of velocity changes (emission of higher frequency waves is expected under abrupt decelerations) and thus, by the re-strengthening rate. Based on our results, cohesive silicate-bearing faults that undergo to frictional melting, also in the presence of liquid water [see natural case discussed by Brantut and Mitchell, 2018] will have the largest re-strengthening rates at the highest power densities (5-15 km depth) and should promote more intense high frequency radiation during slip deceleration. However, according to

Fig. 4, the re-strengthening rates in micro-gabbro are much smaller than those achieved in calcitic-built cohesive rocks. In the latter rocks, if grain-size dependent processes are activated, intense high frequency radiation should occur especially at low power densities (perhaps corresponding to shallow depths, < 2 km) and dry conditions, when re-strengthening rates are the highest (Fig. 4).

5) Conclusions

We performed a series of experiments simulating seismic slip under different environmental conditions (vacuum, room humidity and pressurized water) on two common cohesive crustal rocks (calcitic Carrara marble and micro-gabbro). In general, independently of the environmental conditions, the fault re-strengthening rate at the end of slip is up to one order of magnitude larger in Carrara marble than in micro-gabbro, especially at low power densities (Fig. 4). This large difference in re-strengthening rates is due to the different on-fault deformation processes operating during seismic slip: crystal plastic and grain-size dependent for Carrara marble, melt lubrication for micro-gabbro. The two deformation mechanisms have different constitutive equations and dependence with temperature. With increasing power density, which may correspond to increasing crustal depths, the fault re-strengthening rate becomes almost negligible for Carrara marble whereas it slightly increases for micro-gabbro.

We also found some intriguing second order differences in the magnitude of the re-strengthening rate for the two rock types. These differences are due to the environmental conditions which impact on the efficiency of the particular co-seismic deformation mechanism of the rock. Under vacuum and room-humidity conditions, fault re-strengthening rate at the end of simulated seismic slip in Carrara marble is significantly faster than in the presence of pressurized water, especially at low power densities (Fig. 4). Instead, in micro-gabbro, fault re-

strengthening rate is faster in the presence of pressurized water than under room humidity and vacuum conditions (Fig. 4). We interpreted these well-reproducible second order variations in the re-strengthening rate as the consequence of the change in rate-dependent plasticity in the presence of water for Carrara marble and water-cooling of the frictional interface for micro-gabbro. Our results suggest that both rock composition and presence of water affect the elastic strain energy release rate and the seismic waves radiation pattern during rupture propagation.

Acknowledgments:

This work was funded by the European Research Council Starting Grant project 757290-BEFINE and Consolidator Grant 614705 NOFEAR. We are grateful to S. Nielsen for scientific discussions. We thank P.G. Scarlato for laboratory support. Raw data can be requested from marie.violay@epfl.ch or download at: https://enacshare.epfl.ch/fiaF3NRqUAb8XVgZdjS7wJcuPQeHmGE.

References:

1. Acosta, M., Passelègue, F. X., Schubnel, A., & Violay, M. (2018). Dynamic weakening during earthquakes controlled by fluid thermodynamics. *Nature communications*, *9*(1), 3074.
2. Aubry, J., Passelègue, F. X., Deldicque, D., Girault, F., Marty, S., Lahfid, A., ... & Schubnel, A. (2018). Frictional heating processes and energy budget during laboratory earthquakes. *Geophysical Research Letters*, *45*(22), 12-274.
3. Beeler, N. M., & Tullis, T. E. (1996). Self-healing slip pulses in dynamic rupture models due to velocity-dependent strength. Bulletin of the Seismological Society of America, 86(4), 1130-1148.
4. Boozer, G. D., Hiller, K. H., & Serdengecti, S. (1963). Effects of pore fluids on the deformation behavior of rocks subjected to triaxial compression. Proc. Fifth Sympos. Rock Mechanics. Univ. Minnesota.

5. Brantut N., Mitchell T., 2018 Assessing the efficiency of thermal pressurisation using natural pseudotachylyte-bearing rocks, in press GRL.
6. Brantut, N., Schubnel, A., Rouzaud, J. N., Brunet, F., & Shimamoto, T. (2008). High- velocity frictional properties of a clay- bearing fault gouge and implications for earthquake mechanics. Journal of Geophysical Research: Solid Earth, 113(B10).
7. Brown, K. M., & Fialko, Y. (2012). 'Melt welt'mechanism of extreme weakening of gabbro at seismic slip rates. Nature, 488(7413), 638.
8. Brune, J. N. (1970). Tectonic stress and the spectra of seismic shear waves from earthquakes. Journal of geophysical research, 75(26), 4997-5009.
9. Chang, J. C., Lockner, D. A., & Reches, Z. (2012). Rapid acceleration leads to rapid weakening in earthquake-like laboratory experiments. Science, 338(6103), 101-105.
10. De Paola, N., Holdsworth, R. E., Viti, C., Collettini, C., & Bullock, R. (2015). Can grain size sensitive flow lubricate faults during the initial stages of earthquake propagation?. Earth and Planetary Science Letters, 431, 48-58.
11. Del Gaudio, P., Di Toro, G., Han, R., Hirose, T., Nielsen, S., Shimamoto, T., & Cavallo, A. (2009). Frictional melting of peridotite and seismic slip. Journal of Geophysical Research: Solid Earth, 114(B6).
12. Di Toro, G., Goldsby, D. L., & Tullis, T. E. (2004). Friction falls towards zero in quartz rock as slip velocity approaches seismic rates. Nature, 427(6973), 436.
13. Di Toro, G., Hirose, T., Nielsen, S., Pennacchioni, G., & Shimamoto, T. (2006). Natural and experimental evidence of melt lubrication of faults during earthquakes. science, 311(5761), 647-649.
14. Di Toro, G., Han, R., Hirose, T., De Paola, N., Nielsen, S., Mizoguchi, K., ... & Shimamoto, T. (2011). Fault lubrication during earthquakes. Nature, 471(7339), 494.
15. Di Toro, G., Niemeijer, A., Tripoli, A., Nielsen, S., Di Felice, F., Scarlato, P., ... & Smith, S. (2010). From field geology to earthquake simulation: a new state-of-the-art tool to investigate rock friction during the seismic cycle (SHIVA). Rendiconti Lincei, 21(1), 95-114.
16. Goldsby, D. L., & Tullis, T. E. (2011). Flash heating leads to low frictional strength of crustal rocks at earthquake slip rates. Science, 334(6053), 216-218.
17. Green, H. W., Shi, F., Bozhilov, K., Xia, G., and Reches, Z. 2015. Phase transformation and nanometric flow cause extreme weakening during fault slip. Nature Geoscience 8, 484–489.

18. Han, R., Hirose, T., & Shimamoto, T. (2010). Strong velocity weakening and powder lubrication of simulated carbonate faults at seismic slip rates. Journal of Geophysical Research: Solid Earth, 115(B3).
19. Heaton, T. H. (1990). Evidence for and implications of self-healing pulses of slip in earthquake rupture. Physics of the Earth and Planetary Interiors, 64(1), 1-20.
20. Hirose, T., & Shimamoto, T. (2005). Growth of molten zone as a mechanism of slip weakening of simulated faults in gabbro during frictional melting. Journal of Geophysical Research: Solid Earth, 110(B5).
21. Ida, Y. (1972). Cohesive force across the tip of a longitudinal- shear crack and Griffith's specific surface energy. Journal of Geophysical Research, 77(20), 3796-3805.
22. Kanamori, H. and Rivera, L. (2013). Energy Partitioning During an Earthquake. In Earthquakes: Radiated Energy and the Physics of Faulting (eds R. Abercrombie, A. McGarr, G. Di Toro and H. Kanamori).
23. Liao, Zonghu, Jefferson C. Chang, and Ze'ev Reches. "Fault strength evolution during high velocity friction experiments with slip-pulse and constant-velocity loading." Earth and Planetary Science Letters 406 (2014): 93-101.
24. Latour, S., Campillo, M., Voisin, C., Ionescu, I. R., Schmedes, J., & Lavallée, D. (2011). Effective friction law for small- scale fault heterogeneity in 3D dynamic rupture. Journal of Geophysical Research: Solid Earth, 116(B10).
25. Lockner, D. A., Summers, R., & Byerlee, J. D. (1986). Effects of temperature and sliding rate on frictional strength of granite. In Friction and faulting (pp. 445-469). Birkhäuser, Basel.
26. Lykotrafitis, G., Rosakis, A. J., & Ravichandran, G. (2006). Self-healing pulse-like shear ruptures in the laboratory. Science, 313(5794), 1765-1768.
27. Madariaga, R. (1976). Dynamics of an expanding circular fault. Bulletin of the Seismological Society of America, 66(3), 639-666.
28. Madariaga, R., & Olsen, K. B. (2002). Earthquake dynamics. INTERNATIONAL GEOPHYSICS SERIES, 81(A), 175-194.
29. Marone, C., Raleigh, C. B., & Scholz, C. H. (1990). Frictional behavior and constitutive modeling of simulated fault gouge. Journal of Geophysical Research: Solid Earth, 95(B5), 7007-7025.
30. Marty, S., Passelègue, F. X., Aubry, J., Bhat, H. S., Schubnel, A., & Madariaga, R. (2019). Origin of high- frequency radiation during laboratory earthquakes. *Geophysical Research Letters*.

476 31. McLaskey, G. C., Kilgore, B. D., & Beeler, N. M. (2015). Slip- pulse rupture behavior on a 2 m granite
477 fault. Geophysical Research Letters, 42(17), 7039-7045.
478 32. Nielsen, S., Di Toro, G., Hirose, T., & Shimamoto, T. (2008). Frictional melt and seismic slip. Journal of
479 Geophysical Research: Solid Earth, 113(B1).
480 33. Niemeijer, A., Di Toro, G., Nielsen, S., & Di Felice, F. (2011). Frictional melting of gabbro under extreme
481 experimental conditions of normal stress, acceleration, and sliding velocity. Journal of Geophysical
482 Research: Solid Earth, 116(B7).
483 34. Passelègue, F. X., Goldsby, D. L., & Fabbri, O. (2014). The influence of ambient fault temperature on
484 flash- heating phenomena. Geophysical Research Letters, 41(3), 828-835.
485 35. Perrin, G., Rice, J. R., & Zheng, G. (1995). Self-healing slip pulse on a frictional surface. Journal of the
486 Mechanics and Physics of Solids, 43(9), 1461-1495.
487 36. Peyrat, S., Olsen, K., & Madariaga, R. (2001). Dynamic modeling of the 1992 Landers
488 earthquake. Journal of Geophysical Research: Solid Earth, 106(B11), 26467-26482.
489 37. Platt, J. D., Brantut, N., & Rice, J. R. (2015). Strain localization driven by thermal decomposition during
490 seismic shear. Journal of Geophysical Research: Solid Earth, 120(6), 4405-4433.
491 38. Platt, J. D., Rudnicki, J. W., & Rice, J. R. (2014). Stability and localization of rapid shear in fluid-
492 saturated fault gouge: 2. Localized zone width and strength evolution. Journal of Geophysical Research:
493 Solid Earth, 119(5), 4334-4359.
494 39. Proctor, B. P., Mitchell, T. M., Hirth, G., Goldsby, D., Zorzi, F., Platt, J. D., & Di Toro, G. (2014).
495 Dynamic weakening of serpentinite gouges and bare surfaces at seismic slip rates. Journal of Geophysical
496 Research: Solid Earth, 119(11), 8107-8131.
497 40. Reches, Z. E., & Lockner, D. A. (2010). Fault weakening and earthquake instability by powder
498 lubrication. Nature, 467(7314), 452.
499 41. Reid, H. F. 1910. The mechanism of the earthquake. In The California Earthquake of April 18,1906,
500 Report of the State Earthquake Investigation Commission, Vol. 2. Washington, DC: Carnegie Institution,
501 pp. 1–192.
502 42. Renner, J., Evans, B., & Siddiqi, G. (2002). Dislocation creep of calcite. Journal of Geophysical Research:
503 Solid Earth, 107(B12).

504 43. Rice, J. R., Rudnicki, J. W., & Platt, J. D. (2014). Stability and localization of rapid shear in fluid-
505 saturated fault gouge: 1. Linearized stability analysis. Journal of Geophysical Research: Solid
506 Earth, 119(5), 4311-4333.
507 44. Ruina, A. (1983). Slip instability and state variable friction laws. Journal of Geophysical Research: Solid
508 Earth, 88(B12), 10359-10370.
509 45. Rutter, E. H. (1972). The influence of interstitial water on the rheological behaviour of calcite
510 rocks. Tectonophysics, 14(1), 13-33.
511 46. Rutter, E. H. (1974). The influence of temperature, strain rate and interstitial water in the experimental
512 deformation of calcite rocks. Tectonophysics, 22(3-4), 311-334.
513 47. Rutter, E. H. (1974). The influence of temperature, strain rate and interstitial water in the experimental
514 deformation of calcite rocks. Tectonophysics, 22(3-4), 311-334.
515 48. Segall, P., & Rice, J. R. (2006). Does shear heating of pore fluid contribute to earthquake
516 nucleation?. Journal of Geophysical Research: Solid Earth, 111(B9).
517 49. Schmid, S. M., Panozzo, R., & Bauer, S. (1987). Simple shear experiments on calcite rocks: rheology and
518 microfabric. Journal of structural Geology, 9(5-6), 747-778.
519 50. Schmid, S. M., Paterson, M. S., & Boland, J. N. (1980). High temperature flow and dynamic
520 recrystallization in Carrara marble. Tectonophysics, 65(3-4), 245-280.
521 51. Sibson, R. H., Moore, J. M. M., & Rankin, A. H. (1975). Seismic pumping—a hydrothermal fluid
522 transport mechanism. Journal of the Geological Society, 131(6), 653-659.
523 52. Smith, S. A. F., Nielsen, S., & Di Toro, G. (2015). Strain localization and the onset of dynamic weakening
524 in calcite fault gouge. Earth and Planetary Science Letters, 413, 25-36.
525 53. Stein, S., & Wysession, M. (2009). An introduction to seismology, earthquakes, and earth structure. John
526 Wiley & Sons.
527 54. Sone, H., & Shimamoto, T. (2009). Frictional resistance of faults during accelerating and decelerating
528 earthquake slip. Nature Geoscience, 2(10), 705.
529 55. Spagnuolo, E., Plümper, O., Violay, M., Cavallo, A., & Di Toro, G. (2015). Fast-moving dislocations
530 trigger flash weakening in carbonate-bearing faults during earthquakes. Scientific reports, 5, 16112.
531 56. Spudich, P., Guatteri, M., Otsuki, K., & Minagawa, J. (1998). Use of fault striations and dislocation
532 models to infer tectonic shear stress during the 1995 Hyogo-ken Nanbu (Kobe) earthquake. Bulletin of
533 the Seismological Society of America, 88(2), 413-427.

534 57. Tinti, E., Fukuyama, E., Piatanesi, A., & Cocco, M. (2005). A kinematic source-time function compatible
535 with earthquake dynamics. Bulletin of the Seismological Society of America, 95(4), 1211-1223.
536 58. Tsutsumi, A., & Shimamoto, T. (1997). High- velocity frictional properties of gabbro. Geophysical
537 Research Letters, 24(6), 699-702.
538 59. Verberne, B. A., Niemeijer, A. R., De Bresser, J. H., & Spiers, C. J. (2015). Mechanical behavior and
539 microstructure of simulated calcite fault gouge sheared at 20–600 C: Implications for natural faults in
540 limestones. Journal of Geophysical Research: Solid Earth, 120(12), 8169-8196.
541 60. Violay M., G. Di Toro, S. Nielsen, E. Spagnuolo and J. P. Burg. Thermo-mechanical pressurization of
542 experimental faults in cohesive rocks during seismic slip, in Earth and Planetary Science Letters, vol.
543 429, p. 1-10, 2015.
544 61. Violay, M., Di Toro, G., Gibert, B., Nielsen, S., Spagnuolo, E., Del Gaudio, P., ... & Scarlato, P. G.
545 (2014). Effect of glass on the frictional behavior of basalts at seismic slip rates. Geophysical research
546 letters, 41(2), 348-355.
547 62. Violay, M., Nielsen, S., Gibert, B., Spagnuolo, E., Cavallo, A., Azais, P., ... & Di Toro, G. (2014). Effect
548 of water on the frictional behavior of cohesive rocks during earthquakes. Geology, 42(1), 27-30
549 63. Violay, M., Nielsen, S., Spagnuolo, E., Cinti, D., Di Toro, G., & Di Stefano, G. (2013). Pore fluid in
550 experimental calcite-bearing faults: Abrupt weakening and geochemical signature of co-seismic
551 processes. Earth and planetary science letters, 361, 74-84.
552 64. Walker, A. N., Rutter, E. H., & Brodie, K. H. (1990). Experimental study of grain-size sensitive flow of
553 synthetic, hot-pressed calcite rocks. Geological Society, London, Special Publications, 54(1), 259-284.
554 65. Zoback, M. D., & Harjes, H. P. (1997). Injection- induced earthquakes and crustal stress at 9 km depth
555 at the KTB deep drilling site, Germany. Journal of Geophysical Research: Solid Earth, 102(B8), 18477-
556 18491.
557 66. Zheng, G., & Rice, J. R. (1998). Conditions under which velocity-weakening friction allows a self-healing
558 versus a cracklike mode of rupture. Bulletin of the Seismological Society of America, 88(6), 1466-1483.

559

560

561

562

563

564

565

566

567

568

569

570

571

572

573

574

575

576 **Figures:**

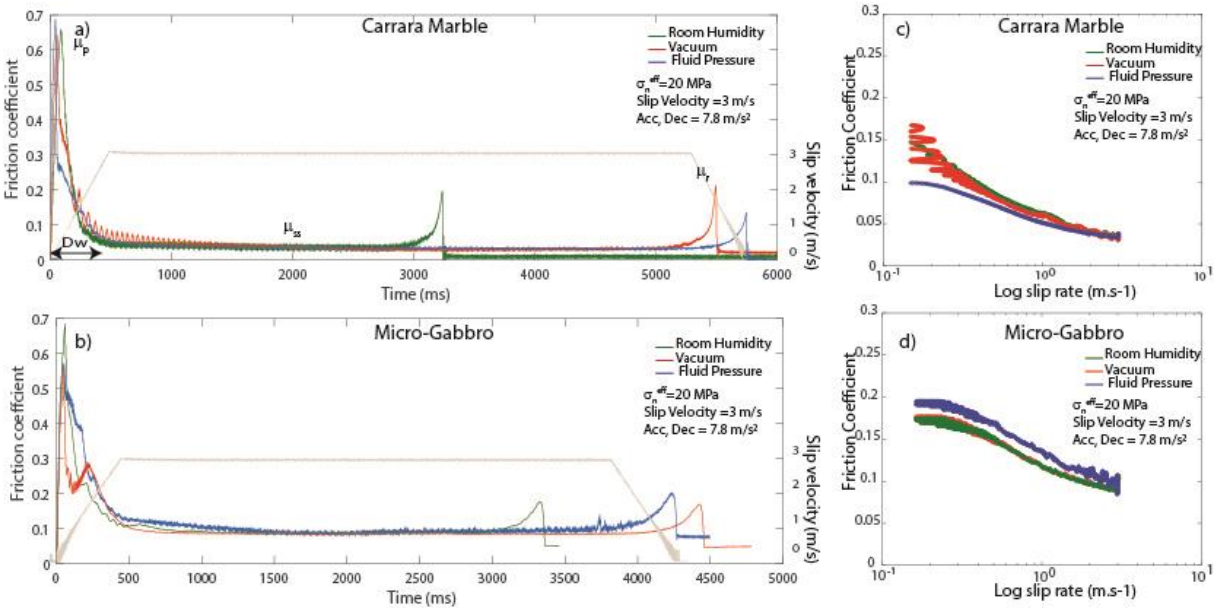

Figure 1. Evolution of the friction coefficient with time and slip rate for Carrara marble and micro-gabbro slid at seismic slip rates. (**a) and (b)** Evolution of the friction coefficient with time in Carrara marble and micro-gabbro. **(c) and (d)** Evolution of the friction coefficient measured during deceleration versus log of the sliding velocity. The experiments were conducted at target velocity V_t = 3 m s^{-1}, acceleration and deceleration = 7.8 m s^{-2}, and σ_n^{eff} = 20 MPa (effective normal stress = $\sigma_n - P_f$). Blue curves (S615 and S567): fluid pressure experiments σ_n = 25 MPa, P_f = 5 MPa; green curves (S307 and S555): room humidity experiments; red curves (S614 and S585): vacuum experiments were run at $P_{vacuum} = 10^{-4}$ mbar. Two examples of sliding velocity function are drawn in grey.

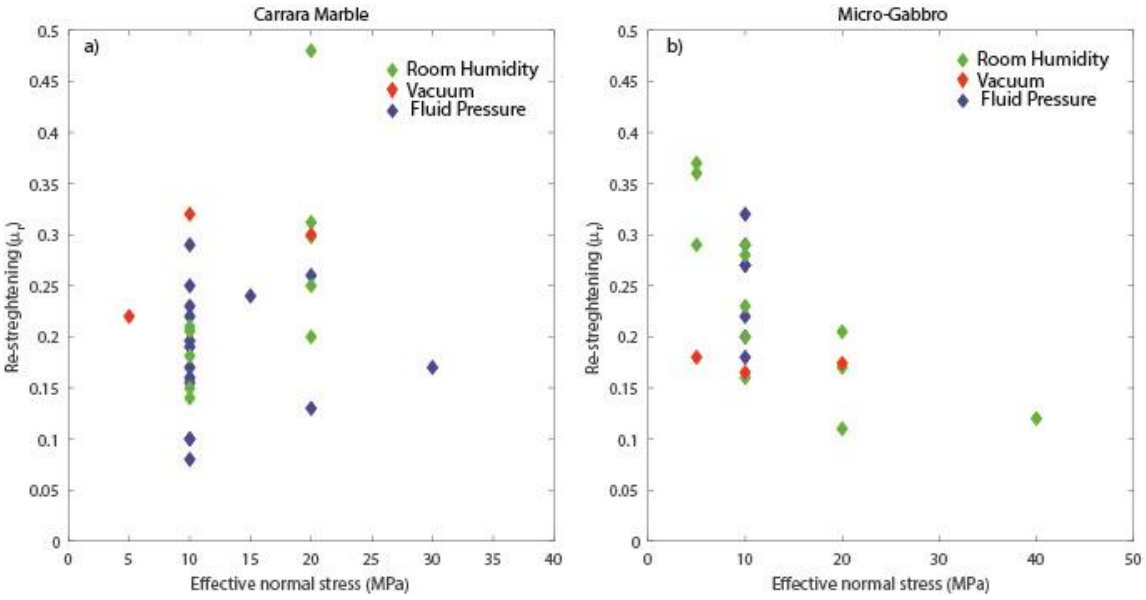

588

589 **Figure 2.** Influence of σ_n^{eff} on the re-strenghtening for **(a)** Carrara Marble and **(b)** micro-gabbro.

590 Blue dots: fluid pressure experiments; green dots: room humidity experiments; red dots:

591 vacuum experiments $P_{vacuum} = 10^{-4}$ mbar.

592

593

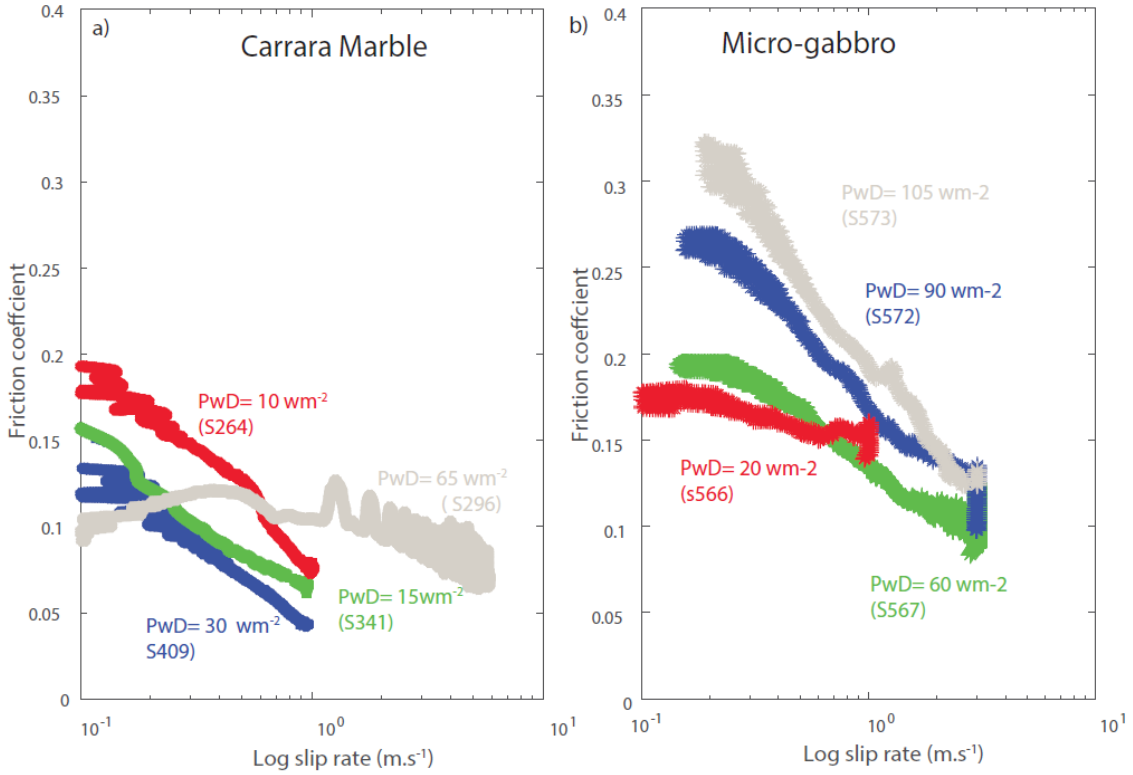

Figure 3. Evolution of the friction coefficient during slip deceleration versus log of the sliding velocity for **(a)** Carrara marble (S409, S341, S296, S264) and **(b)** micro-grabbro (S566, S567, S572 and S573). Experiments were conducted at different power density ($\sigma_n^{eff} \cdot Vt$). Target velocity (Vt) ranging from 1 and 6.5 m s^{-1}, acceleration and deceleration = 7.8 m s^{-2}, and σ_n^{eff} from 10 to 30 MPa (effective normal stress= $\sigma_n - P_f$). The experiments were all performed under fluid pressure conditions (P_f= 5 MPa).

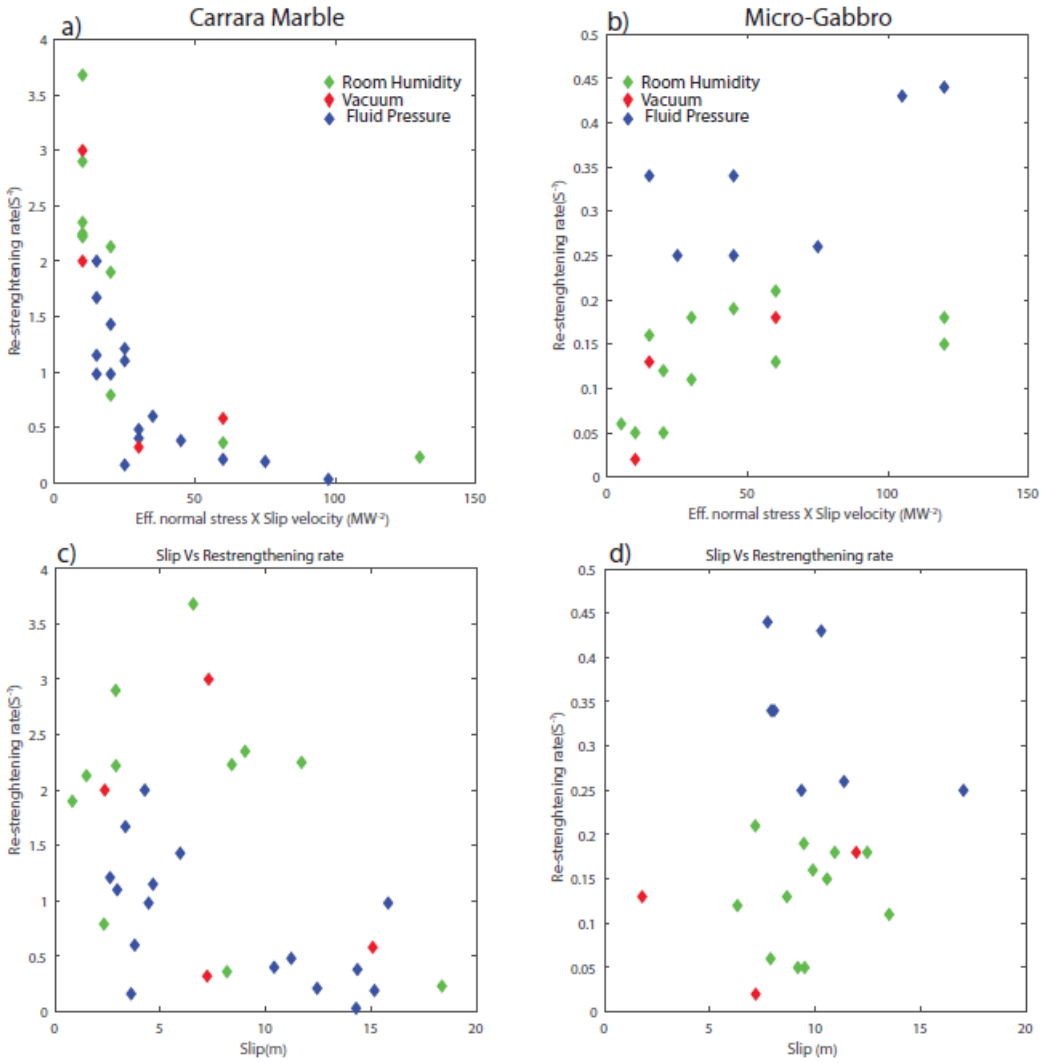

Figure 4. Influence of power density **(a,b)** ($\sigma_n^{eff} \cdot Vt$) and slip **(c, d)** on the friction re-strengthening rate. Blue dots: fluid pressure experiments; green dots: room humidity experiments; red dots: vacuum experiments $P_{vacuum} = 10^{-4}$ mbar.

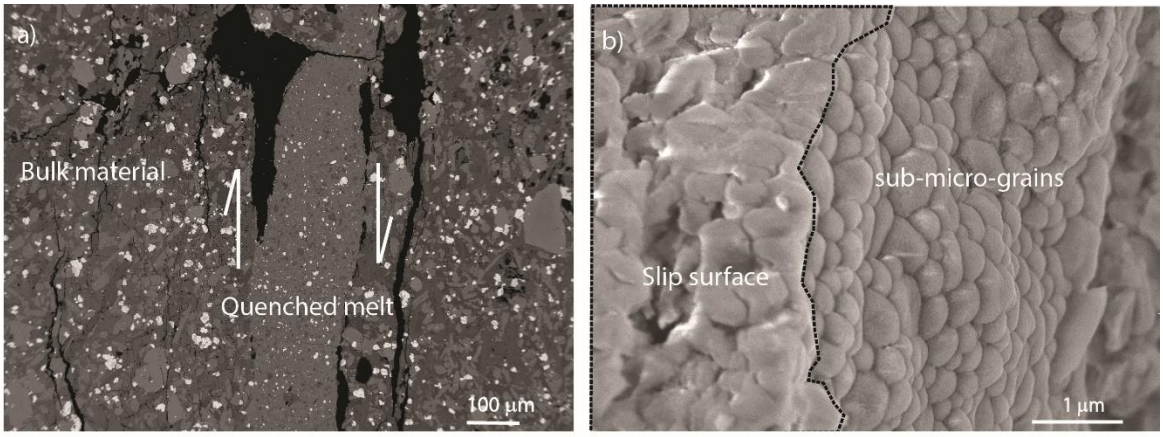

606 **Figure 5.** Microstructural observations of experimental slip surfaces and slipping zones after
607 shearing. **(a)** Slipping zone after an experiment performed on micro-gabbro (s585, V = 3 m s^{-1},
608 σ_n= 20 MPa, Vacuum conditions see also Violay et al., 2014). The slipping zone is made by
609 quenched melt (i.e., glass matrix, see composition in Table 2) which wraps grains of plagioclase
610 and pyroxene that survived from frictional melting (Scanning Electron Microscope, back scatter
611 electron image). **(b)** Slip surface after an experiment performed on calcitic Carrara marble
612 (s614, V = 3 m s^{-1}, σ_n= 20 MPa, Vacuum conditions, see Violay et al., 2014). The slip surface
613 is made by micro- to nano-grains of calcite and lime. Small decarbonation vacuoles decorate
614 the recrystallized calcite grains (Scanning Electron Microscope, secondary electron image).

615

616

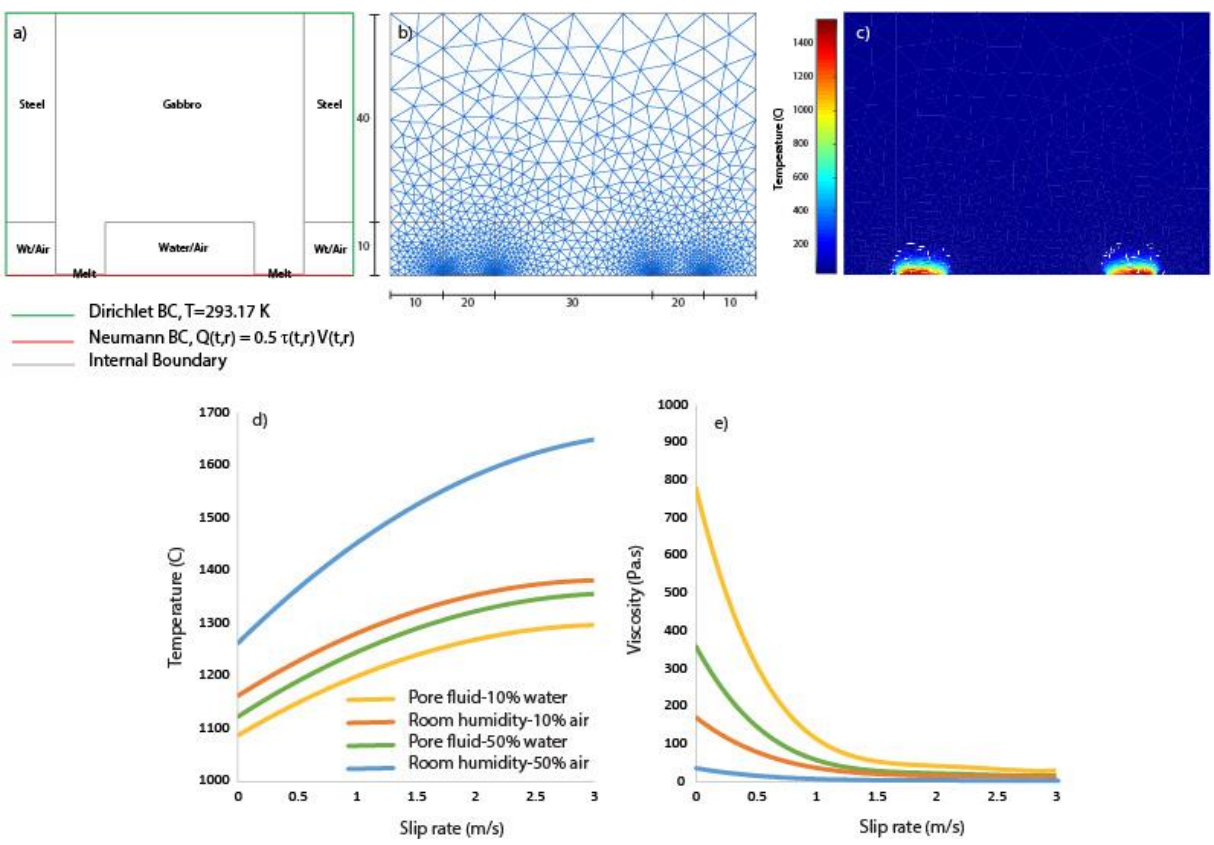

617

618 **Figure 6.** FEM 2D time dependent heat diffusion model. **(a,b)** Model geometry with description
619 of the Boundary Conditions and mesh geometry. **(c)** The snapshot of the temperature
620 distribution at the end of the experiment s585 conducted on gabbro. **(d)** Temperature evolution

621 of the slip zone during slip deceleration (t_r-t_{ss}). **(e)** Melt viscosity evolution during slip
622 deceleration.

623

624

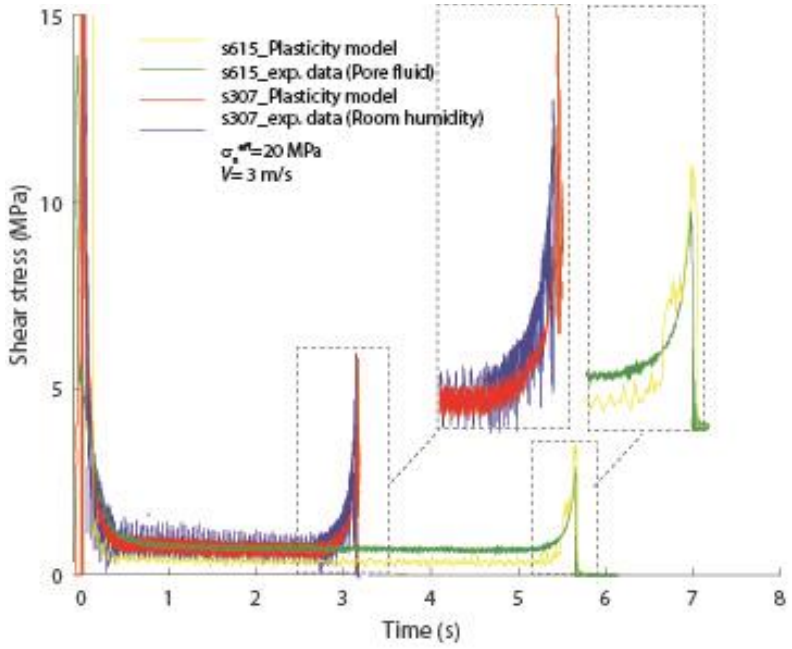

625

626 **Figure 7.** Results of the 1D time dependent heat diffusion model fully coupled with diffusion
627 creep flow law for both room humidity (blue and red curves) and pore fluid (green and yellow
628 curves) conditions.

629

	Micro-Gabbro	Carrara Marble	Water	Air	Melt	Steel
K [10 ^-6 m2/s]	0.8	1.48	0.15	1.5	0.344	4.2
ρ [kg/m3]	2990	2700	1000	1.2	2591	2000
C [J/(kgK)]	949	700	4200	1000	1484	460

630 **Table 1.** Thermal properties of the fluid (air and water) and micro-gabbro used in the FEM
631 numerical model, as well as the thermal properties of Carrara marble used for the coupled

632 diffusion model and plasticity flow law. K = thermal conductivity, ρ = density, C = specific
633 heat. Φ the liquid fraction.

Sample	Micro-Gabbro	s585	
Phase	crystalline	glass	s.d.
#		7	
Al_2O_3	14.27	15.68	0.74
Na_2O	4.49	4.26	0.91
CaO	9.22	10.21	1.43
SiO_2	45.48	45.22	0.90
K_2O	2.71	2.71	0.57
MgO	7.15	6.88	0.57
P_2O_5	1.88	1.14	0.14
FeO	10.28	8.31	0.34
TiO_2	3.02	2.88	0.38
MnO	0.19	0.17	0.05
Total	98.69	97.46	

634 **Table 2.** Chemical composition of the micro-gabbro (XRD) and of the glass for experiment
635 S585 performed under vacuum conditions (Electron Microprobe Analysis). The analysis does
636 not close to about 100% because only Fe2+ was determined.